Aalto University

OPEN ACCESS

This is an electronic reprint of the original article.
This reprint may differ from the original in pagination and typographic detail.

Amini, Mohammad; Fumega, Adolfo O.; González-Herrero, Héctor; Vaňo, Viliam; Kezilebieke, Shawulienu; Lado, Jose L.; Liljeroth, Peter

Atomic-Scale Visualization of Multiferroicity in Monolayer NiI_2

Published in:
Advanced Materials

DOI:
10.1002/adma.202311342

Published: 02/05/2024

Document Version
Publisher's PDF, also known as Version of record

Published under the following license:
CC BY

Please cite the original version:
Amini, M., Fumega, A. O., González-Herrero, H., Vaňo, V., Kezilebieke, S., Lado, J. L., & Liljeroth, P. (2024). Atomic-Scale Visualization of Multiferroicity in Monolayer NiI_2. *Advanced Materials*, *36*(18), Article 2311342. https://doi.org/10.1002/adma.202311342

This material is protected by copyright and other intellectual property rights, and duplication or sale of all or part of any of the repository collections is not permitted, except that material may be duplicated by you for your research use or educational purposes in electronic or print form. You must obtain permission for any other use. Electronic or print copies may not be offered, whether for sale or otherwise to anyone who is not an authorised user.

Check for updates

ADVANCED MATERIALS
www.advmat.de

Atomic-Scale Visualization of Multiferroicity in Monolayer NiI_2

Mohammad Amini, Adolfo O. Fumega, Héctor González-Herrero, Viliam Vaňo, Shawulienu Kezilebieke, Jose L. Lado, and Peter Liljeroth**

Progress in layered van der Waals materials has resulted in the discovery of ferromagnetic and ferroelectric materials down to the monolayer limit. Recently, evidence of the first purely 2D multiferroic material was reported in monolayer NiI_2. However, probing multiferroicity with scattering-based and optical bulk techniques is challenging on 2D materials, and experiments on the atomic scale are needed to fully characterize the multiferroic order at the monolayer limit. Here, scanning tunneling microscopy (STM) supported by density functional theory (DFT) calculations is used to probe and characterize the multiferroic order in monolayer NiI_2. It is demonstrated that the type-II multiferroic order displayed by NiI_2, arising from the combination of a magnetic spin spiral order and a strong spin-orbit coupling, allows probing the multiferroic order in the STM experiments. Moreover, the magnetoelectric coupling of NiI_2 is directly probed by external electric field manipulation of the multiferroic domains. The findings establish a novel point of view to analyze magnetoelectric effects at the microscopic level, paving the way toward engineering new multiferroic orders in van der Waals materials and their heterostructures.

1. Introduction

Multiferroics are materials that exhibit simultaneously more than one ferroic order.[1–3] Over the past years, numerous studies have reported different bulk multiferroics, most of them complex oxides.[4–7] Multiferroics can be classified based on the presence of weak or strong coupling between the orders as type I or type II, respectively.[2,3] In the particular case of magnetic and ferroelectric orders, type-II multiferroics showing a strong magnetoelectric coupling[8,9] have a huge potential for technological applications including spintronics, data storage, and efficient energy management in computation.[10–12] Nevertheless, multiferroics displaying a strong magnetoelectric coupling at sufficiently high temperatures to build functional devices remain elusive.

The dawn of 2D materials has enabled new strategies for the design of artificial multiferroics.[13] The weak van der Waals bonding between the layers allows to easily reach the 2D limit with these compounds, thus obtaining families of building blocks with different properties.[14–22] These can be stacked and twisted in heterostructures, leading to a wide range of emergent phenomena including multiferroicity.[23–28] Recently, it was suggested that the multiferroicity of the bulk van der Waals compound NiI_2 remains in the mechanically-exfoliated few-layer[29] and monolayer limits.[30] Theoretical analyses have addressed the origin of this type-II multiferroic order to the combination of the magnetic spin-spiral order of NiI_2 and the strong spin-orbit (SOC) coupling of the I atoms.[31] To provide experimental evidence of 2D

M. Amini, A. O. Fumega, H. González-Herrero, V. Vaňo, J. L. Lado, P. Liljeroth
Department of Applied Physics
Aalto University
Aalto FI-00076, Finland
E-mail: jose.lado@aalto.fi; peter.liljeroth@aalto.fi

H. González-Herrero
Departamento de Física de la Materia Condensada
Universidad Autónoma de Madrid
Madrid E-28049, Spain

H. González-Herrero
Condensed Matter Physics Center (IFIMAC)
Universidad Autónoma de Madrid
Madrid E-28049, Spain

V. Vaňo
Joseph Henry Laboratories and Department of Physics
Princeton University
Princeton, NJ 08544, USA

S. Kezilebieke
Department of Physics
Department of Chemistry and Nanoscience Center
University of Jyväskylä
Jyväskylä FI-40014, Finland

The ORCID identification number(s) for the author(s) of this article can be found under https://doi.org/10.1002/adma.202311342

© 2024 The Authors. Advanced Materials published by Wiley-VCH GmbH. This is an open access article under the terms of the Creative Commons Attribution License, which permits use, distribution and reproduction in any medium, provided the original work is properly cited.

DOI: 10.1002/adma.202311342

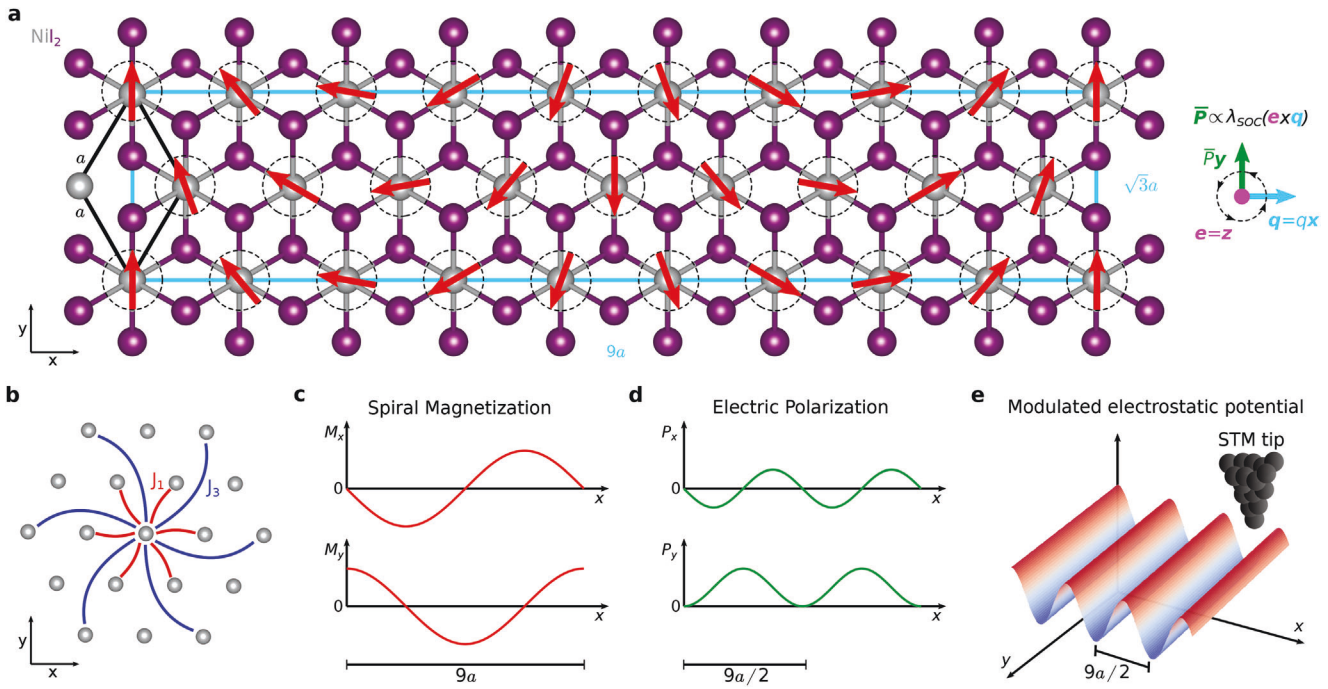

Figure 1. Origin of multiferroicity in monolayer NiI_2. a) Unit cell of monolayer NiI_2. $9a \times \sqrt{3}a$ supercell is required to describe the magnetic spin-spiral order with propagation vector **q** in the *x*-direction and rotation vector **e** in the z-direction. The presence of spin-orbit coupling λ_{SOC} induces a net electric polarization $\overline{P}$ in the y-direction. b) Ferromagnetic first neighbor J_1 and antiferromagnetic third neighbor J_3 magnetic exchange interactions between Ni atoms giving rise to the spin spiral order in the monolayer. c) Magnetization components of the spin spiral showing a periodicity of $9a$ in the *x*-direction. d) Electric polarization components associated with the magnetic spin spiral in the presence of SOC showing a periodicity of $9a/2$ in the *x*-direction. e) Modulated electrostatic potential that can be probed with an STM. It shows a $9a/2$ periodicity in the *x*-direction as a consequence of the multiferroic order.

multiferroicity, circular dichroic Raman, birefringence, and second-harmonic-generation measurements on both mono- and multi-layer NiI_2 were performed, establishing NiI_2 as the first purely 2D multiferroic with a transition temperature $T_C = 21$ K.[30] However, optical measurements might not suffice to demonstrate the emergent ferroelectricity in the 2D limit.[32] In addition, typical bulk techniques used to identify the magnetic spin spiral and to measure the electric polarization that gives rise to the multiferroic order, cannot be applied in the monolayer limit.[33–35] These factors suggest that the origin of the multiferroic order in monolayer NiI_2 has not been experimentally established and its full characterization requires measurements at the microscopic level.

In this work, we present real-space visualization of the multiferroicity in monolayer NiI_2. We show that the magnetoelectric coupling present in this kind of type-II multiferroics allows us to directly probe and characterize the multiferroic order by scanning tunneling microscopy (STM). These results are supported by non-collinear ab initio calculations based on density functional theory (DFT) in monolayer NiI_2. Moreover, we provide evidence of the magnetoelectric coupling of this 2D system by electrical manipulation of the multiferroic domains. Our findings demonstrate the visualization of multiferroic order in van der Waals materials with atomic-scale resolution, establishing a strategy that can be further applied to artificial multiferroic van der Waals heterostructures.

2. Results and Discussion

2.1. Multiferroic Order in NiI_2

In bulk, NiI_2 displays a magnetic spin spiral at low temperatures.[33,34] DFT calculations have determined that the **q** vector characterizing the spin spiral order in bulk is a consequence of the competition between magnetic exchange interactions between Ni atoms.[31,36,37] In particular, ferromagnetic intralayer first-neighbor J_1, antiferromagnetic intralayer third-neighbor J_3, and antiferromagnetic interlayer second-neighbor $\tilde{J}_2$ magnetic exchange interactions are the most relevant. These interactions lead to a **q** vector in bulk whose in-plane component lies on the $\overline{\Gamma M}$ segment in reciprocal space, and whose value can be modified by external parameters, such as pressure, that change the ratio between the different magnetic exchanges.[36,38] In the monolayer limit, there are no interlayer interactions, hence the **q** vector is determined by the competition between J_1 and J_3 (**Figure 1b**). DFT calculations have predicted that in this scenario the **q** vector lies on the $\overline{\Gamma K}$ segment in reciprocal space, corresponding to the third-neighbor bond direction.[39] The classical Heisenberg model solution predicts that $\mathbf{q} = (q, q, 0)$, with q in units of the reciprocal lattice of the structural single-unit cell with lattice vector **a**, is determined by the J_1/J_3 ratio.[40,41]

Apart from the magnetic order, theoretical analyses have shown that monolayer NiI_2 develops a ferroelectric polarization

© 2024 The Authors. Advanced Materials published by Wiley-VCH GmbH

15214095, 2024, 18, Downloaded from https://advanced.onlinelibrary.wiley.com/doi/10.1002/adma.202311342 by Aalto University, Wiley Online Library on [15/01/2025]. See the Terms and Conditions (https://onlinelibrary.wiley.com/terms-and-conditions) on Wiley Online Library for rules of use; OA articles are governed by the applicable Creative Commons License

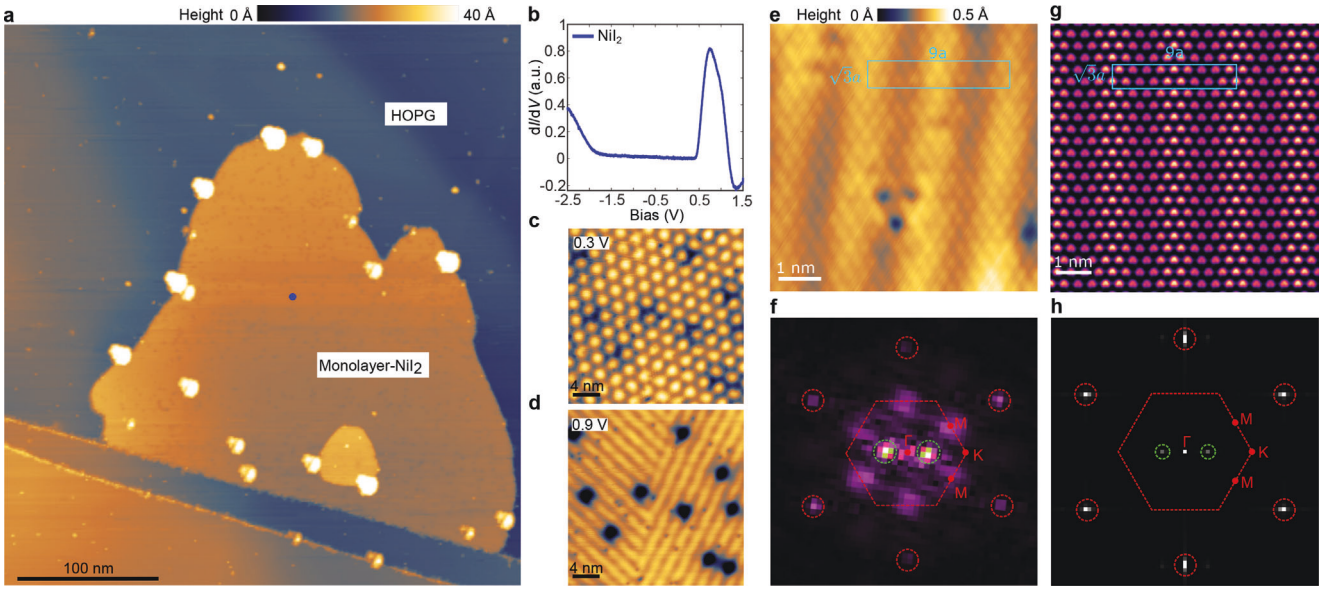

Figure 2. Characterization of monolayer NiI_2. a) Large area STM scan of monolayer NiI_2 on HOPG (image size: 370 × 400 nm^2, V = 1.2 V, I = 4 pA). b) dI/dV point spectra measured on monolayer NiI_2 (blue dot shown in panel a). c,d) Small-area STM images of monolayer NiI_2 at 0.3 V and 0.9 V, respectively (image size: 25 × 25 nm^2). e,f) Atomic resolution STM scan of monolayer NiI_2 (image size 6.5 × 6.5 nm^2, V = 0.43 V, I = 100 pA) and corresponding FFT. g,h) DFT-computed STM image at the conduction band of monolayer NiI_2 and corresponding FFT. In the real space images, the light blue rectangle depicts the unit cell of the commensurate spin spiral shown in Figure 1a. In contrast to the theory, the experimental stripes are not aligned precisely with the atomic lattice. In the FFT images, the red-circled peaks correspond to the single unit cell giving rise to the depicted Brillouin zone, while the green-circled peaks are associated with the ferroelectric modulation.

due to the combination of this spin spiral order and the strong spin-orbit coupling of the I atoms.[31] These results are based on the theoretical derivation for the emergence of ferroelectricity in spiral magnets.[42] This approach predicts that a net ferroelectric polarization $\overline{\mathbf{P}}$, which is proportional to the SOC strength λ_{SOC}, arises perpendicular to the $\mathbf{q}$ and $\mathbf{e}$ rotation vector that characterizes the spin spiral (as shown in Figure 1a). At the more microscopic level, this relationship shows that given a spin spiral with magnetization $\mathbf{M} = \mathrm{M}(-\sin(\mathbf{qr}), \cos(\mathbf{qr}), 0)$ in cartesian coordinates (Figure 1c) the emergent electric polarization is given by

$$\mathbf{P} = \Lambda \frac{\mathbf{M} \times (\nabla \times \mathbf{M})}{\mathrm{M}^2}, \tag{1}$$

where Λ is proportional to λ_{SOC} and some physical constants.[43] Equation (1) leads to $\mathbf{P} = \Lambda \mathrm{q}(-\sin(2\mathbf{q} \cdot \mathbf{r})/2, \sin^2(\mathbf{q} \cdot \mathbf{r}), 0)$ for the given spin spiral $\mathbf{M}$. The spatial average of this equation leads to a net polarization $\overline{\mathbf{P}}$ with non-zero components only in the direction perpendicular to the $\mathbf{q}$ and $\mathbf{e}$ vectors.[42,43] Equation (1) shows that the emergent electric polarization has a real space modulation whose periodicity is half of the periodicity of the spin spiral (Figure 1d).

The modulation of the induced ferroelectric order, which is produced by the coupling between spin and charge degrees of freedom, is the property that can be used to characterize the multiferroic order of monolayer NiI_2 with an STM. The emergence of ferroelectricity is accompanied by ferroelectric displacements of the atomic positions in the directions of the electric polarizations and results in the emergence of a modulated electrostatic potential. This electrostatic potential displays the same periodicity as the ferroelectric polarization and modulates the energy bands of NiI_2. The modulation results in an observable contrast in STM images, thus providing a signature of the multiferroic order allowing its characterization (Figure 1e). Importantly, note that the STM does not resolve the P_y and the P_x components of the polarization. Instead, STM can resolve the electrostatic potential generated by the non-uniform emergent electric polarization. The magnetoelectric coupling occurring in this multiferroic allows the visualization of the magnetic spin spiral periodicity without the need to use more complex spin-polarized scanning microscopy techniques.[44,45]

2.2. STM Characterization of Monolayer NiI_2

Figure 2a shows a large area STM scan of our sample (see Experimental Section for details on sample preparation). It reveals the presence of a well-formed monolayer NiI_2 on HOPG. The dI/dV spectrum of monolayer NiI_2 is shown in Figure 2b. The valence and conduction bands can be distinguished at −1.9 V and 0.4 V, respectively, indicating that NiI_2 is an insulator with a gap of 2.3 eV. The negative conductance occurring at high bias can be associated with the resonant tunneling through confined energy levels within the 2D layer.[46] Figure 2c,d shows small-area STM images at 0.3 V (within the NiI_2 bandgap) and at 0.9 V (within the NiI_2 conduction band). A systematic analysis with scans at different energies can be found in the Supporting Information. Inside the gap, the contrast is not affected by the polarization of the NiI_2, and we observe a hexagonal moiré modulation arising from the lattice mismatch between HOPG and NiI_2 (Figure 2c). However, as the conduction band is modulated by the ferroelectric polarization, the stripe-like pattern expected for this kind of

© 2024 The Authors. Advanced Materials published by Wiley-VCH GmbH

15214095, 2024, 18, Downloaded from https://advanced.onlinelibrary.wiley.com/doi/10.1002/adma.202311342 by Aalto University, Wiley Online Library on [15/01/2025]. See the Terms and Conditions (https://onlinelibrary.wiley.com/terms-and-conditions) on Wiley Online Library for rules of use; OA articles are governed by the applicable Creative Commons License

type-II multiferroic appears at biases corresponding to the NiI_2 conduction band (Figure 2d). Two distinct regions with different stripe orientations can be observed. These correspond to two different multiferroic domains. Finally, there are different types of atomic scale defects that are analyzed in detail in the Supporting Information.

Figure 2e shows an atomic-resolution scan in a single domain region, the FFT of this scan is shown in Figure 2f. The spin-spiral **q** vector can be determined from the relationship between the single unit cell $a \times a$ and the stripe modulation. From our experimental results, we obtain $a = 3.85$ Å for monolayer NiI_2. The periodicity of the stripes is $L_S = 17.8$ Å corresponding to about $4.6a$. According to Equation (1) the modulation of the stripes caused by the emergent electric polarization displays at half the periodicity of the spin spiral (Figure 1c,d), leading to a spin spiral periodicity of $9.2a$ in the experiment. The spin-spiral **q** vector can be directly extracted from the peaks associated with the stripes in the FFT (green circles in Figure 2f) as half of the peak value. We have obtained **q** = (0.069, 0.041, 0) in units of the reciprocal lattice vectors, showing a small deviation from $\overline{\Gamma K}$ segment expected for the $J_1 - J_3$ spin model. The projection in the $\overline{\Gamma K}$ segment is $0.173\overline{\Gamma K}$, corresponding to **q** = (0.057, 0.057, 0). It can be observed that this small variation in the experimental **q** vector from the $\overline{\Gamma K}$ segment leads to a small tilt (≈4.6°) of the stripe modulation (Figure 2f). This effect could be a consequence of local defects in the sample, the proximity of other multiferroic domains, or the influence of other parameters such as intralayer second-neighbor magnetic exchange, or biquadratic interactions not considered in the $J_1 - J_3$ spin model.[41,47] In particular, it has been highlighted that the Kitaev interaction plays a major role in stabilizing the **q** vector observed in bulk.[47] However, based on the phase diagrams obtained in that work, the different **q** vector that we have measured in the monolayer should lie in the regime dominated by the J_1 and J_3 parameters, in agreement with recent theoretical works.[39] Other spin-orbit coupling interactions such as Dzyaloshinskii-Moriya interaction may compete with Kitaev interactions, due to the explicit breaking of mirror symmetry in our system. Finally, the diffuse peaks around the M points are associated with the defect seen in the scan. The analysis of the filtered FFT images is shown in the Supporting Information.

Extracting the information on the spin spiral from the STM measurements allows us to model monolayer NiI_2 using DFT. Neglecting the small tilt in the ferroelectric modulation, the unit cell describing the multiferroic order in monolayer NiI_2 can be well approximated by the commensurate $9a \times \sqrt{3}a$ supercell shown in Figure 1a, corresponding to **q** = (0.064, 0.064, 0) and $\sqrt{3}/9\overline{\Gamma K} \sim 0.192\overline{\Gamma K}$. From the experimental **q** = (0.057, 0.057, 0) we can estimate $J_3/J_1 = -0.263$.[40,41] This result shows that monolayer NiI_2 is on the verge of a spin-spiral to ferromagnetic transition ($J_3/J_1 = -0.25$),[41] which might explain why in some studies the presence of ferroelectric polarization was only reported down to the bilayer limit but not in the monolayer.[29] An important factor to consider could be the effect of the substrate. Song et al. grew monolayer NiI_2 on hBN and found evidence of multiferroic behavior,[30] while Ju et al. grew NiI_2 on SiO_2 and did not report multiferroicity in the single layer limit.[29] Our results on monolayer NiI_2 on HOPG show multiferroic order. Therefore, the substrate could have a critical influence not only on the presence of multiferroicity but also on its order parameters. A comparison of the experimental **q** vector based on our experiments with previous theoretical predictions for free-standing monolayer NiI_2, could point out that DFT tends to overestimate the $|J_3/J_1|$ ratio.[38,39] This could be rationalized by the typical limitations of the different DFT functionals to deal with electronic correlations and electronic localization, thus introducing an overestimation of the long-range magnetic exchanges. This could explain why "ab initio" calculations predict a spin spiral for $NiCl_2$ while the observed ground state is ferromagnetic.[39] Nevertheless, the effect of the substrate on the multiferroic order of NiI_2 should be further analyzed to reconcile the different experimental and theoretical works.

In order to shed light on the microscopic origin of the STM modulation observed in the experiments, we have performed non-collinear DFT calculations in the commensurate $9a \times \sqrt{3}a$ supercell and the **q** = (0.064, 0.064, 0) spin spiral (see Experimental Section for computational details). When SOC is included in the atomic relaxations, we observe the emergence of ferroelectric forces that drive the atoms to new positions following the same periodicity as the electric polarization (Figure 1d). Due to this symmetry breaking in real space, the computed STM image (Figure 2g) and its FFT (Figure 2h) display a modulation with the periodicity of the electric polarization, i.e., half of the magnetic spiral, in a good agreement with the experimental observations.

Having characterized the spiral order of monolayer NiI_2, we now proceed to determine the strength of the ferroelectric polarization. The image contrast over the stripes depends on the bias voltage, i.e., at a certain bias voltage, the maximum (minimum) in the local electric polarization corresponds to a bright (dark) area of the stripe pattern, while at a different bias, the opposite will occur. A more convenient way to analyze where the minima and maxima of the local electric polarization are located is by considering the band bending of the conduction band. Local variations of the electric polarization, such as those encountered on the edges of ferroelectric islands, induce a local energy band bending that can be used to estimate the strength of the electric polarization.[48–50] The emergence of an inhomogeneous electric polarization in NiI_2 is expected to produce similar band bendings, but in this case within the same multiferroic domain and with the periodicity of the ferroelectric modulation (Figure 1d). This behavior is experimentally demonstrated and theoretically reproduced in **Figure 3**.

Figure 3b shows dI/dV spectra recorded along a line in a single domain region (green arrow shown in Figure 3a) parallel to the **q** vector. Figure 3e shows the DFT simulated line spectra for the commensurate $9a \times \sqrt{3}a$ supercell and the **q** = (0.064, 0.064, 0) spin spiral. Both plots show the conduction bands. A clear underestimation of the bandgap is observed for the DFT calculations, which is typical for the LDA approximation. However, both experiment and theory show a band bending modulation of the conduction band that becomes more apparent when analyzing the dI/dV spectra at a maximum and a minimum of the stripe modulation in Figure 3c (spectra taken at the positions indicated by the blue and red dots in Figure 3a, respectively). A clear shift in energies between these two positions occurs as a consequence of the ferroelectric modulation introducing a band bending. The shift in energies is also seen in the DFT calculations (Figure 3f). At a bias of 1 V (Figure 3a), this shift produces a higher intensity

© 2024 The Authors. Advanced Materials published by Wiley-VCH GmbH

15214095, 2024, 18, Downloaded from https://advanced.onlinelibrary.wiley.com/doi/10.1002/adma.202311342 by Aalto University, Wiley Online Library on [15/01/2025]. See the Terms and Conditions (https://onlinelibrary.wiley.com/terms-and-conditions) on Wiley Online Library for rules of use; OA articles are governed by the applicable Creative Commons License

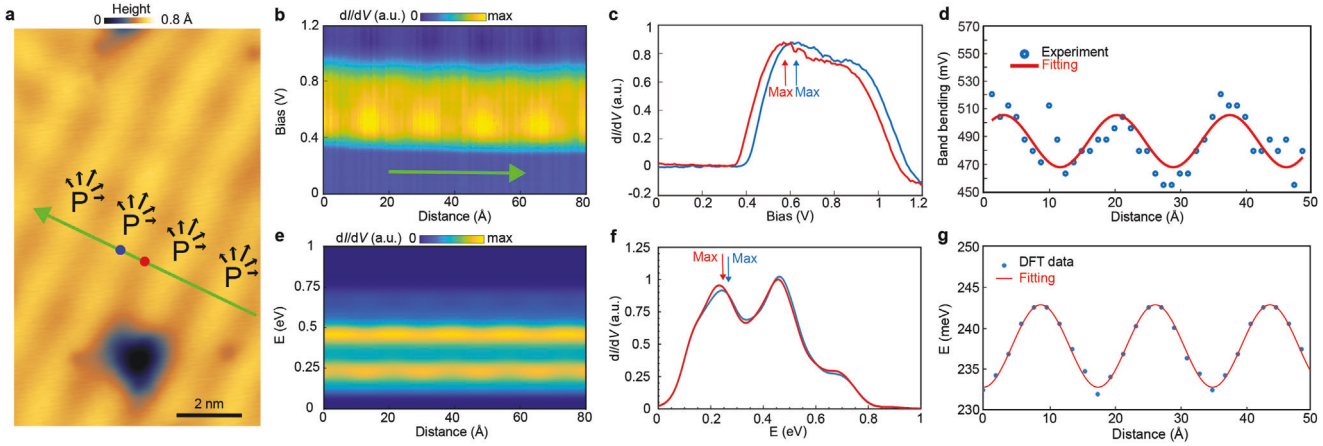

Figure 3. Probing electric polarization in NiI_2. a) Small area STM scan showing a multiferroic domain where a line spectrum was performed along the green arrow ($V = 1$ V, $I = 100$ pA). Red and blue dots show the 0 and maximum polarization, respectively. The small black arrows indicate both the direction and strength of the local electric polarization. b) dI/dV line spectrum capturing the conduction band of monolayer NiI_2 along the green arrow in panel (a) parallel to the **q** vector. c) dI/dV spectra showing the shift in energy between a maximum and a minimum of the stripe modulation (blue and red dots in panel (a)). d) dI/dV intensity maximum of the bottom of the conduction band along the green line showing a modulated band bending as a consequence of the ferroelectric modulation. e–g) Corresponding DFT calculations for panels (b–d) computed in the $9a \times \sqrt{3}a$ supercell and the **q** = (0.064, 0.064, 0) spin spiral.

in the areas where the local polarization is maximal (blue line in Figure 3c) compared to where the polarization is zero (red line in Figure 3c). This allows us to resolve the local polarization for the stripe pattern (black arrows in Figure 3a). However, note that there is a 180° ambiguity in the determination of the direction of this local polarization.

The band bending can be analyzed by tracking the shift in the differential conductance maxima as a function of the position across the modulation. This is shown in Figure 3d,g for the experimental and theoretical data, respectively. First, we should stress that DFT in the LDA approximation underestimates the energy gap,[51] which is a well-known issue in DFT. In addition, it is difficult to capture the band alignment with the substrate quantitatively. Therefore, the absolute energy position of the conduction bands should be treated as a free parameter when comparing theory and experiment. However, this does not affect the prediction of electric polarization. The important point is to compare the cosine modulation produced by the emergent electric polarization. The observed oscillatory behavior can be fitted to $E = E_0 + E_P \sin(2\pi x/L_S + \phi)$, where E_0 corresponds to an average of the differential conductance maximum at the bottom of the conduction band, E_P is the band bending modulation caused by the inhomogeneous emergent polarization, L_S is the stripe periodicity that has already been analyzed and, ϕ is a trivial phase related to the starting point considered for the fitting. We obtain E_P = 16.8 mV from the experiment and E_P = 5.0 meV from the DFT calculation. This underestimation of the ab initio calculations could be a consequence of the limitations of the LDA approximation for the atomic relaxations. However, apart from this small difference, the qualitative agreement between theory and experiment is remarkable. For phonon-driven ferroelectrics such as SnSe and SnTe, STM experiments have shown the band bending is on the order of several hundreds of meV[48–50,52] and an associated electric polarization $P \approx 10^{-10}$ C m^{-1} has been estimated.[49,52] Therefore, considering that in monolayer NiI_2 we observe a band bending of 1 or 2 orders of magnitude smaller, a $P \approx 10^{-12}$ C m^{-1} can be estimated for monolayer NiI_2 However, this is a local value that corresponds to the maximum amplitude of the electric polarization. An across-the-stripes spatial average needs to be performed to compare with transport measurements. This yields an estimate of the polarization of $\bar{P} \simeq 5 \times 10^{-13}$ C m^{-1}. As a reference, it is interesting to compare this value to the one reported for bulk.[35] There, transport measurements report a value for the in-plane volumetric electric polarization in the bulk of 150×10^{-6} C m^{-2}. This corresponds to an in-plane electric polarization per layer of $\bar{P}_{bulk} = 10^{-13}$ C m^{-1}, consistent with our estimations. Note that the different dimensionality as well as substrate effects in our case can explain the difference between our estimate and the bulk measurement.

2.3. Manipulation of Multiferroic Domain Boundaries

We have also directly probed the magnetoelectric coupling in monolayer NiI_2 by external electric field manipulation of the multiferroic domains. **Figure** 4a–d shows the movement of the multiferroic domain wall induced by voltage pulses from the STM tip (the bias is swept from 1 to 4 V with a closed feedback loop and a current set point of 100 pA). Starting in Figure 4a, the multiferroic domain wall (black-dashed line) and different kinds of defects (highlighted with circles, detailed analysis in the Supporting Information) can be identified. The neutral defects (pink circle) can be used as a spatial reference for the domain manipulation. A first voltage pulse is performed in the position indicated by the sky blue dot (in the left domain) and it leads to the configuration shown in Figure 4b. We can observe that the domain wall has moved to the right increasing the size of the left domain. Moreover, a clear difference between the different types of defects can be observed. While the charged defects are mobile, the neutral ones do not move and can be used as a reference to

© 2024 The Authors. Advanced Materials published by Wiley-VCH GmbH

15214095, 2024, 18, Downloaded from https://advanced.onlinelibrary.wiley.com/doi/10.1002/adma.202311342 by Aalto University, Wiley Online Library on [15/01/2025]. See the Terms and Conditions (https://onlinelibrary.wiley.com/terms-and-conditions) on Wiley Online Library for rules of use; OA articles are governed by the applicable Creative Commons License

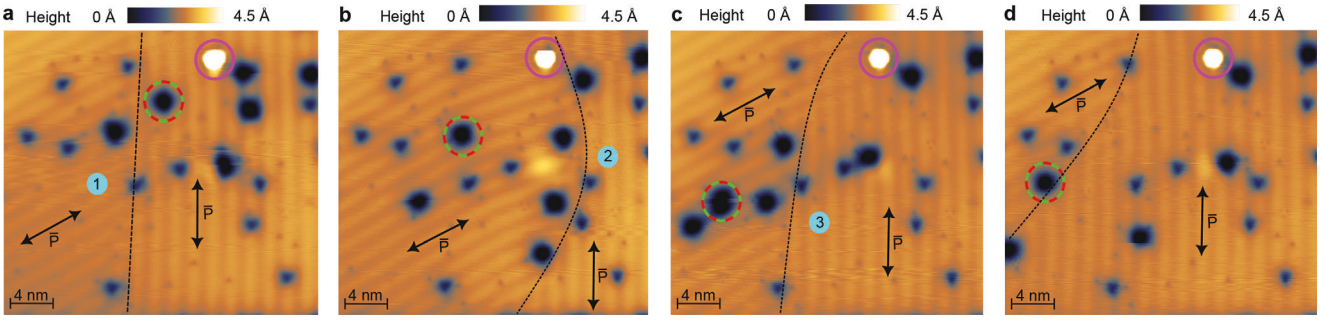

Figure 4. Manipulation of multiferroic domains. a–d) Using voltage pulses from the tip (sweeping the bias from 1 to 4 V with closed feedback loop) to manipulate the multiferroic domains (image size 30×27 nm^2, $V = 1$ V, $I = 20$ pA). Sky blue dots mark the position of the tip during the process and the numbers on them track the order of events. The black-dashed lines highlight the domain boundary, the pink circle shows a neutral defect on the surface used as a spacial reference, and the dashed red-and-green circle corresponds to a type of mobile charge defect. The black arrows show the direction of the average polarization $\bar{P}$ in each domain. The 180° ambiguity in its determination is highlighted.

analyze the domain manipulation. After the scan shown in Figure 4b, we applied a second voltage pulse in the right domain leading to Figure 4c, and a third one leading to Figure 4d. As before, the location of the domain wall moves away from the position of the voltage pulse and charged defects are mobile, while neutral ones are not. Ferroelectric domain wall manipulation through voltage pulses had been achieved before in ferroelectric SnTe.[50] Now, we show here that multiferroic domains in this kind of magnetic spin-spiral multiferroics are also tunable by external electric fields, thus showing direct evidence of the magnetoelectric coupling in monolayer NiI_2.

3. Conclusion

In conclusion, we have probed and characterized the multiferroic order in monolayer NiI_2 down to the atomic scale. Using a combination of STM experiments and non-collinear ab initio calculations, we show that in this spin-spiral SOC-driven multiferroic, the emergent ferroelectric polarization induces a modulation of the electrostatic potential. This is directly reflected in the local density of states allowing its direct visualization by STM. This modulation has half of the spin-spiral periodicity, allowing us to characterize the spin-spiral vector as $\mathbf{q} = (0.069, 0.041, 0)$ and the parameter relation $J_3/J_1 = -0.263$ of the associated spin model. The observed band bending allows us to estimate the polarization $P \approx 10^{-12}$ C m^{-1} for monolayer NiI_2. Finally, we have probed the magnetoelectric coupling of NiI_2 by manipulating the multiferroic domains by local electric fields induced by the STM tip. Our results firmly establish the atomic scale origin of multiferroicity in NiI_2 and pave the way for future studies on multiferroics and 2D van der Waals materials at the microscopic level.

4. Experimental Section

Sample Preparation: NiI_2 was grown by molecular beam epitaxy (MBE) on highly oriented pyrolytic graphite (HOPG) under ultra-high vacuum conditions (UHV, base pressure $\approx 1 \times 10^{-10}$ mbar). Initial preparation of the HOPG substrate involved multiple cleaving steps to ensure cleanliness of the surface, followed by outgassing at $T \approx 300$ °C for one hour to remove any remaining surface contamination. After that, the substrate temperature was stabilized at ≈100 °C for the growth of monolayer NiI_2. For the growth, two sources of material were used: Ni (rod with 99.999% purity) was evaporated using an electron-beam evaporator while iodine was deposited from a Knudsen cell using NiI_2 (anhydrous powder, 99.95% purity) as an iodine source (NiI_2 decomposes at a temperature of around ≈400 °C). The sample was grown in an iodine background pressure of $\approx 9 \times 10^{-8}$ mbar and the growth duration was 30 min. After the growth, the sample was annealed for 5 min in an iodine background. Two factors were critical to the successful growth of NiI_2: the precise control of substrate temperature and maintaining an iodine pressure consistently above $\approx 7 \times 10^{-8}$ mbar.

STM Measurements: After the preparation, the sample was inserted into the low-temperature STM (CreaTec LT-STM) connected to the same UHV system, and subsequent experiments were performed at $T = 4.7$ K. STM images were taken in the constant-current mode. dI/dV spectra were recorded by standard lock-in detection while sweeping the sample bias in an open feedback loop configuration, with a peak-to-peak bias modulation specified for each measurement and at a frequency of 515 Hz.

Computational Details: Ab initio electronic structure calculations based on density functional theory[53] (DFT) were performed in monolayer NiI_2. Calculations were carried out with the all-electron full-potential linearized augmented-plane-wave method, using a fully non-collinear formalism with spin-orbit coupling (SOC) as implemented in Elk.[54] The local density approximation (LDA) was used for the exchange-correlation functional.[55] The results presented were converged with respect to all the parameters, considering the $9a \times \sqrt{3}a$ supercell and the $\mathbf{q} = (0.064, 0.064, 0)$ spin spiral, a $2 \times 6 \times 1$ k-mesh, and a vacuum spacing of 20 Å. Relaxations of the atomic positions in the spin spiral state including SOC require careful convergence of the forces (10^{-4} a.u) and the Kohn-Sham potential (10^{-7} a.u). The DFT STM images were computed in a 312×60 real space mesh and interpolated to a finer orthogonal mesh (800×800) to obtain a higher resolution STM image and to compute the FFT.

Supporting Information

Supporting Information is available from the Wiley Online Library or from the author.

Acknowledgements

M.A. and A.O.F. contributed equally to this work. This research made use of the Aalto Nanomicroscopy Center (Aalto NMC) facilities and was supported by the European Research Council (ERC-2017-AdG no. 788185 "Artificial Designer Materials" and ERC-2021-StG no. 101039500 "Tailoring Quantum Matter on the Flatland") and Academy of Finland (Academy professor funding nos. 318995 and 320555, Academy research fellow nos. 331342, 336243 and nos. 338478 and 346654, and Academy postdoctoral fellow no. 349696). Computing resources from the Aalto Science-IT

© 2024 The Authors. Advanced Materials published by Wiley-VCH GmbH

15214095, 2024, 18, Downloaded from https://advanced.onlinelibrary.wiley.com/doi/10.1002/adma.202311342 by Aalto University, Wiley Online Library on [15/01/2025]. See the Terms and Conditions (https://onlinelibrary.wiley.com/terms-and-conditions) on Wiley Online Library for rules of use; OA articles are governed by the applicable Creative Commons License

project and CSC Helsinki are gratefully acknowledged. V.V. acknowledges fellowship support from the Princeton Center for Complex Materials supported by NSF-DMR-2011750.

Conflict of Interest

The authors declare no conflict of interest.

Data Availability Statement

The data that support the findings of this study are available from the corresponding author upon reasonable request.

Keywords

density-functional theory calculations, magneto electric coupling, multiferroic order, scanning tunneling microscopy, two-dimensional multiferroics

Received: October 28, 2023
Revised: January 9, 2024
Published online: February 5, 2024

[1] N. A. Hill, *J. Phys. Chem. B* **2000**, *104*, 6694.
[2] M. Fiebig, T. Lottermoser, D. Meier, M. Trassin, *Nat. Rev. Mater.* **2016**, *1*, 16046.
[3] N. A. Spaldin, R. Ramesh, *Nat. Mater.* **2019**, *18*, 203.
[4] T. Kimura, T. Goto, H. Shintani, K. Ishizaka, T. Arima, Y. Tokura, *Nature* **2003**, *426*, 55.
[5] N. Hur, S. Park, P. A. Sharma, J. S. Ahn, S. Guha, S.-W. Cheong, *Nature* **2004**, *429*, 392.
[6] M. Gajek, M. Bibes, S. Fusil, K. Bouzehouane, J. Fontcuberta, A. Barthélémy, A. Fert, *Nat. Mater.* **2007**, *6*, 296.
[7] C.-W. Nan, M. I. Bichurin, S. Dong, D. Viehland, G. Srinivasan, *J. Appl. Phys.* **2008**, *103*, 031101.
[8] M. Fiebig, *J. Phys. D: Appl. Phys.* **2005**, *38*, R123.
[9] M. Matsubara, S. Manz, M. Mochizuki, T. Kubacka, A. Iyama, N. Aliouane, T. Kimura, S. L. Johnson, D. Meier, M. Fiebig, *Science* **2015**, *348*, 1112.
[10] D. Pantel, S. Goetze, D. Hesse, M. Alexe, *Nat. Mater.* **2012**, *11*, 289.
[11] J.-M. Hu, L.-Q. Chen, C.-W. Nan, *Adv. Mater.* **2015**, *28*, 15.
[12] P. Schoenherr, S. Manz, L. Kuerten, K. Shapovalov, A. Iyama, T. Kimura, M. Fiebig, D. Meier, *npj Quantum Mater.* **2020**, *5*, 86.
[13] A. K. Geim, I. V. Grigorieva, *Nature* **2013**, *499*, 419.
[14] Z. Fei, B. Huang, P. Malinowski, W. Wang, T. Song, J. Sanchez, W. Yao, D. Xiao, X. Zhu, A. F. May, W. Wu, D. H. Cobden, J.-H. Chu, X. Xu, *Nat. Mater.* **2018**, *17*, 778.
[15] B. Huang, G. Clark, E. Navarro-Moratalla, D. R. Klein, R. Cheng, K. L. Seyler, D. Zhong, E. Schmidgall, M. A. McGuire, D. H. Cobden, W. Yao, D. Xiao, P. Jarillo-Herrero, X. Xu, *Nature* **2017**, *546*, 270.
[16] J.-U. Lee, S. Lee, J. H. Ryoo, S. Kang, T. Y. Kim, P. Kim, C.-H. Park, J.-G. Park, H. Cheong, *Nano Lett.* **2016**, *16*, 7433.
[17] C. Gong, L. Li, Z. Li, H. Ji, A. Stern, Y. Xia, T. Cao, W. Bao, C. Wang, Y. Wang, Z. Q. Qiu, R. J. Cava, S. G. Louie, J. Xia, X. Zhang, *Nature* **2017**, *546*, 265.
[18] Z. Zhang, J. Shang, C. Jiang, A. Rasmita, W. Gao, T. Yu, *Nano Lett.* **2019**, *19*, 3138.
[19] M. M. Ugeda, A. J. Bradley, Y. Zhang, S. Onishi, Y. Chen, W. Ruan, C. Ojeda-Aristizabal, H. Ryu, M. T. Edmonds, H.-Z. Tsai, A. Riss, S.-K. Mo, D. Lee, A. Zettl, Z. Hussain, Z.-X. Shen, M. F. Crommie, *Nat. Phys.* **2015**, *12*, 92.
[20] S. C. de la Barrera, M. R. Sinko, D. P. Gopalan, N. Sivadas, K. L. Seyler, K. Watanabe, T. Taniguchi, A. W. Tsen, X. Xu, D. Xiao, B. M. Hunt, *Nat. Commun.* **2018**, *9*, 1427.
[21] C. Cui, W.-J. Hu, X. Yan, C. Addiego, W. Gao, Y. Wang, Z. Wang, L. Li, Y. Cheng, P. Li, X. Zhang, H. N. Alshareef, T. Wu, W. Zhu, X. Pan, L.-J. Li, *Nano Lett.* **2018**, *18*, 1253.
[22] S. Yuan, X. Luo, H. L. Chan, C. Xiao, Y. Dai, M. Xie, J. Hao, *Nat. Commun.* **2019**, *10*, 1775.
[23] Y. Cao, V. Fatemi, A. Demir, S. Fang, S. L. Tomarken, J. Y. Luo, J. D. Sanchez-Yamagishi, K. Watanabe, T. Taniguchi, E. Kaxiras, R. C. Ashoori, P. Jarillo-Herrero, *Nature* **2018**, *556*, 80.
[24] Y. Cao, V. Fatemi, S. Fang, K. Watanabe, T. Taniguchi, E. Kaxiras, P. Jarillo-Herrero, *Nature* **2018**, *556*, 43.
[25] S. Kezilebieke, M. N. Huda, V. Vaňo, M. Aapro, S. C. Ganguli, O. J. Silveira, S. Głodzik, A. S. Foster, T. Ojanen, P. Liljeroth, *Nature* **2020**, *588*, 424.
[26] V. Vaňo, M. Amini, S. C. Ganguli, G. Chen, J. L. Lado, S. Kezilebieke, P. Liljeroth, *Nature* **2021**, *599*, 582.
[27] M. Haavisto, J. L. Lado, A. O. Fumega, *SciPost Phys.* **2022**, *13*, 052.
[28] A. O. Fumega, J. L. Lado, *2D Mater.* **2023**, *10*, 025026.
[29] H. Ju, Y. Lee, K.-T. Kim, I. H. Choi, C. J. Roh, S. Son, P. Park, J. H. Kim, T. S. Jung, J. H. Kim, K. H. Kim, J.-G. Park, J. S. Lee, *Nano Lett.* **2021**, *21*, 5126.
[30] Q. Song, C. A. Occhialini, E. Ergeçen, B. Ilyas, D. Amoroso, P. Barone, J. Kapeghian, K. Watanabe, T. Taniguchi, A. S. Botana, S. Picozzi, N. Gedik, R. Comin, *Nature* **2022**, *602*, 601.
[31] A. O. Fumega, J. L. Lado, *2D Mater.* **2022**, *9*, 025010.
[32] Y. Jiang, Y. Wu, J. Zhang, J. Wei, B. Peng, C.-W. Qiu, *Nature* **2023**, *619*, E40.
[33] D. Billerey, C. Terrier, N. Ciret, J. Kleinclauss, *Phys. Lett. A* **1977**, *61*, 138.
[34] S. Kuindersma, J. Sanchez, C. Haas, *Physica B+C* **1981**, *111*, 231.
[35] T. Kurumaji, S. Seki, S. Ishiwata, H. Murakawa, Y. Kaneko, Y. Tokura, *Phys. Rev. B* **2013**, *87*, 014429.
[36] K. Riedl, D. Amoroso, S. Backes, A. Razpopov, T. P. T. Nguyen, K. Yamauchi, P. Barone, S. M. Winter, S. Picozzi, R. Valentí, *Phys. Rev. B* **2022**, *106*, 035156.
[37] J. Kapeghian, D. Amoroso, C. A. Occhialini, L. G. P. Martins, Q. Song, J. S. Smith, J. J. Sanchez, J. Kong, R. Comin, P. Barone, B. Dupé, M. J. Verstraete, A. S. Botana, *arXiv* **2023**, arXiv:2306.04729.
[38] C. A. Occhialini, L. G. P. Martins, Q. Song, J. S. Smith, J. Kapeghian, D. Amoroso, J. J. Sanchez, P. Barone, B. Dupé, M. j. Verstraete, J. Kong, A. S. Botana, R. Comin, *arXiv* **2023**, arXiv:2306.11720.
[39] J. Sødequist, T. Olsen, *2D Mater.* **2023**, *10*, 035016.
[40] S. Hayami, S.-Z. Lin, C. D. Batista, *Phys. Rev. B* **2016**, *93*, 184413.
[41] C. Glittum, O. F. Syljuåsen, *Phys. Rev. B* **2021**, *104*, 184427.
[42] M. Mostovoy, *Phys. Rev. Lett.* **2006**, *96*, 067601.
[43] J. Hu, *Phys. Rev. Lett.* **2008**, *100*, 077202.
[44] J. Repicky, P.-K. Wu, T. Liu, J. P. Corbett, T. Zhu, S. Cheng, A. S. Ahmed, N. Takeuchi, J. Guerrero-Sanchez, M. Randeria, R. K. Kawakami, J. A. Gupta, *Science* **2021**, *374*, 1484.
[45] P. Schoenherr, J. Müller, L. Köhler, A. Rosch, N. Kanazawa, Y. Tokura, M. Garst, D. Meier, *Nat. Phys.* **2018**, *14*, 465.
[46] C. Song, H. Mao, Y. Yang, X. Liu, Z. Yin, Z. Hu, K. Wu, J. Zhang, *Adv. Funct. Mater.* **2022**, *32*, 2105256.
[47] X. Li, C. Xu, B. Liu, X. Li, L. Bellaiche, H. Xiang, *Phys. Rev. Lett.* **2023**, *131*, 036701.
[48] K. Chang, J. Liu, H. Lin, N. Wang, K. Zhao, A. Zhang, F. Jin, Y. Zhong, X. Hu, W. Duan, Q. Zhang, L. Fu, Q.-K. Xue, X. Chen, S.-H. Ji, *Science* **2016**, *353*, 274.

© 2024 The Authors. Advanced Materials published by Wiley-VCH GmbH

15214095, 2024, 18, Downloaded from https://advanced.onlinelibrary.wiley.com/doi/10.1002/adma.202311342 by Aalto University, Wiley Online Library on [15/01/2025]. See the Terms and Conditions (https://onlinelibrary.wiley.com/terms-and-conditions) on Wiley Online Library for rules of use; OA articles are governed by the applicable Creative Commons License

[49] K. Chang, F. Küster, B. J. Miller, J.-R. Ji, J.-L. Zhang, P. Sessi, S. Barraza-Lopez, S. S. P. Parkin, *Nano Lett.* **2020**, *20*, 6590.
[50] M. Amini, O. J. Silveira, V. Vaňo, J. L. Lado, A. S. Foster, P. Liljeroth, S. Kezilebieke, *Adv. Mater.* **2023**, *35*, 2206456.
[51] R. M. Martin, *Electronic Structure: Basic Theory and Practical Methods*, Cambridge University Press, Cambridge, UK **2004**.
[52] K. Chang, T. P. Kaloni, H. Lin, A. Bedoya-Pinto, A. K. Pandeya, I. Kostanovskiy, K. Zhao, Y. Zhong, X. Hu, Q.-K. Xue, X. Chen, S.-H. Ji, S. Barraza-Lopez, S. S. P. Parkin, *Adv. Mater.* **2019**, *31*, 1804428.
[53] P. Hohenberg, W. Kohn, *Phys. Rev.* **1964**, *136*, B864.
[54] Elk code, http://elk.sourceforge.net/, (accessed: June 2023).
[55] W. Kohn, L. J. Sham, *Phys. Rev.* **1965**, *140*, A1133.

© 2024 The Authors. Advanced Materials published by Wiley-VCH GmbH

15214095, 2024, 18, Downloaded from https://advanced.onlinelibrary.wiley.com/doi/10.1002/adma.202311342 by Aalto University, Wiley Online Library on [15/01/2025]. See the Terms and Conditions (https://onlinelibrary.wiley.com/terms-and-conditions) on Wiley Online Library for rules of use; OA articles are governed by the applicable Creative Commons License